Ultramicroscopy 288 (2027) 114462

Contents lists available at ScienceDirect

Ultramicroscopy

journal homepage: www.elsevier.com/locate/ultramic

Controlling charge, energy spread, and pulse duration in an ultrafast scanning electron microscope

Tomáš Chlouba [a,*,1], Magdalena Solà-Garcia [a,1], Nika van Nielen [a,1], Matthias Wilts-Liebtrau [a], Julian Litzel [b], Leon Brückner [b], Roy Shiloh [b,c], Erik Kieft [d], Pieter Kruit [e], Peter Hommelhoff [b,f], Albert Polman [a]

[a] Center for Nanophotonics, AMOLF, Science Park 104, 1098 XG Amsterdam, Amsterdam, The Netherlands
[b] Physics Department, Friedrich-Alexander-Universität Erlangen-Nürnberg (FAU), Erlangen, Germany
[c] Institute of Applied Physics, Hebrew University of Jerusalem (HUJI), Jerusalem, Israel
[d] Thermo Fisher Scientific, Achtseweg Noord 5, 5651 GG Eindhoven, Eindhoven, The Netherlands
[e] Department of Imaging Physics, Delft University of Technology, Lorentzweg 1, 2628CJ, Delft, The Netherlands
[f] Faculty of Physics, Ludwig Maximilian University Munich, D-80799, Munich, Germany

ARTICLE INFO

Keywords:
Ultrafast scanning electron microscopy
Boersch effect
Schottky feg
Dielectric laser acceleration
Retarding field analyzer

ABSTRACT

Ultrafast photoemission scanning electron microscopes (USEMs) enable time-resolved and light–matter interaction experiments within a versatile SEM platform. However, the interplay between cathode excitation wavelength, extractor voltage, and electron-optical settings leads to complex trade-offs between charge per pulse, energy spread, pulse duration, and spatial resolution. Here, we systematically investigate these dependencies in a modified Schottky field-emission SEM driven by a 300 femtosecond laser pulses at 345 nm and 258 nm with a pulse repetition rate of 1 MHz. Using a custom retarding field analyzer and dielectric laser accelerator-based temporal cross-correlation measurements, we quantify the evolution of energy width, electron pulse duration, and emitted charge across a wide parameter space. We identify three distinct operational regimes: (i) a high-extractor voltage regime providing optimal spatial resolution but limited charge per pulse, (ii) an intermediate regime enabling rapid suppression of thermionic background and nominally better energy resolution, and (iii) a low-extractor voltage, high-current regime supporting tens to hundreds of electrons per pulse or alternatively ultralow intrinsic energy spread at the expense of spatial resolution. The energy spread exhibits a linear dependence on bunch charge consistent with space-charge (Boersch) broadening, while intrinsic sub-eV energy widths down to 0.15 eV are achieved under optimized conditions. These results establish the operational parameter space of ultrafast photoemission SEMs and provide practical guidelines for tailoring beam parameters to applications including PINEM spectroscopy, dielectric laser acceleration, and general electron–light interaction experiments.

1. Introduction

Electron microscopy has been a cornerstone of materials science for nearly a century. From its earliest implementations to modern aberration-corrected instruments capable of resolving individual atoms, the technique has undergone continuous refinement. In scanning electron microscopy (SEM), a focused electron beam is rastered across a sample and secondary electrons are collected to form an image, whereas in transmission electron microscopy (TEM), transmitted electrons are detected carrying structural information of thin specimens [1,2].

Beyond structural imaging, electron microscopes rapidly evolved into multifunctional analytical platforms. A variety of auxiliary detection schemes, such as cathodoluminescence (CL), energy-dispersive X-ray spectroscopy (EDX), electron energy-loss spectroscopy (EELS), and electron diffraction (ED), enable chemical, electronic, and crystallographic characterization while maintaining the spatial resolution of the primary probe. In each case, the same electron probe is employed; only the detected signal differs.

* Corresponding author.
E-mail address: t.chlouba@amolf.nl (T. Chlouba).
[1] These authors contributed equally.

https://doi.org/10.1016/j.ultramic.2026.114462
Received 19 May 2026; Received in revised form 9 October 2026; Accepted 18 October 2026
Available online 19 October 2026
0304-3991/© 2026 The Authors. Published by Elsevier B.V. This is an open access article under the CC BY license (http://creativecommons.org/licenses/by/4.0/).

More recently, access to the temporal degree of freedom has expanded the capabilities of electron microscopy even further. In time-resolved electron microscopy, electron pulses down to sub-ps durations are generated either by chopping the initial electron beam by electrostatic beam blanking [3,4] or through the photoemission of electrons from the electron gun when excited with a pulsed laser beam [4–13], leading to sub-ps electron pulses. This high temporal resolution enables the study of ultrafast dynamics in diffraction [14], holography [15] and carrier dynamics [10], among others. Moreover, it is possible to optically excite the sample in a synchronized way, enabling the direct probing of local optical near fields [16–24]. This later approach, known as photon-induced near-field electron microscopy (PINEM), has emerged as a powerful tool in nanophotonics.

Beyond microscopy, electron beams have emerged as versatile tools for exploring fundamental electron-light-matter interactions. The well-defined and controllable interaction between free electrons and optical fields enables studies of quantum entanglement [25], the implementation of electron-based qubits [26–28], generation of attosecond electron pulses for probing sub-cycle dynamics [23,24,29–31], and the development of on-chip laser-driven particle accelerators [32–44].

For many of these applications, maintaining the high spatial resolution of the electron microscope is no longer the primary concern and other parameters, like the energy spread of the electron beam [23,45–47] or the total number of particles in a single bunch [40,48,49] become the parameter to optimize for. In photoemission SEM these parameters can be controlled by adjusting several electron gun and photoemission settings. One of those is the wavelength of the laser pulse that triggers the initial electron emission. Another is the setting of the gun itself, by the voltages on the extractor plate and condenser lenses. A combination of these can give access to different gun regimes which can boost the charge per bunch up to even hundreds of electrons or alternatively achieve very low energy spread, depending on the needs of a particular experiment.

In this work we investigated the properties of a pulsed electron beam generated with a laser-driven Schottky cathode. In particular we study the energy width, pulse length, charge per bunch as a function of driving wavelength, laser power, extractor voltage and condenser lens voltages. Because the performance of SEMs depends sensitively on column alignment, emitter condition, and electron-optical design, the exact quantitative values reported here should be interpreted within the context of the specific instrument used. For example, the photoemission efficiency depends strongly on emitter age and cooling history, and optimal extractor voltages, and therefore also condenser lens voltages, vary between individual Schottky tips. Rather than providing universally applicable absolute numbers, our results establish operational trends and practical guidelines for tailoring ultrafast electron beam parameters to the requirements of a given experiment.

2. Experimental

A schematic of the ultrafast scanning electron microscope (USEM) is shown in Fig. 1a. The instrument is based on a Thermo Fisher Quanta 250 FEG that was modified to provide optical access to the electron cathode through a UV-transparent window. The cathode consists of a ZrO/W Schottky tip with a work function of $\phi \approx 2.9$ eV. The tip protrudes slightly from a negatively biased suppressor electrode (V_{supp}), which suppresses emission from off-axis regions and confines electron emission to the apex. A positive voltage, relative to the cathode, is applied to the extractor electrode beneath the tip (V_{ext}), reducing the surface potential barrier via the Schottky effect and thereby facilitating electron emission. In standard continuous operation, the cathode is heated to approximately 1800 K via Ohmic heating, promoting the population of higher-energy states in the cathode and thereby increasing the number of electrons with sufficient energy to overcome the emission barrier.

Downstream of the extractor electrode, two condenser lenses (known in electron microscopy convention as the C1 and C2 lenses) form the initial electron-optical system of the column. Together, these lenses

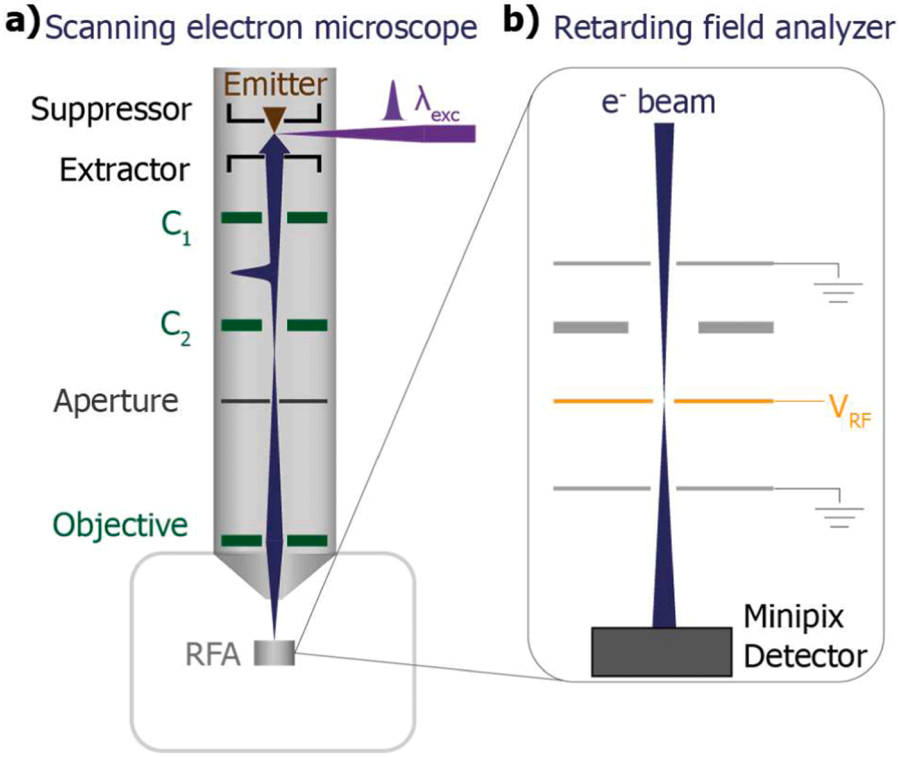

Fig. 1. (a) Schematic of the USEM setup. A fs laser beam excites a Schottky emitter to generate electron pulses. The electron beam goes through a set of lenses and is focused onto the retarding field analyzer (RFA), which is placed in the sample plane. (b) Schematic of the RFA setup. The electron beam is focused onto the retarding electrode, the retarding voltage V_{RF} is then scanned around the voltage of the beam while the transmitted electrons are detected downstream by the Minipix detector.

project an image of the virtual source onto a fixed crossover plane located several centimetres above the aperture plate. The selected aperture (in our case always 70 μm diameter) then spatially filters the beam, and the downstream optics project the crossover image onto the specimen.

For a given extractor voltage, the voltages applied to C1 and C2 determine the effective magnification of the source onto the fixed crossover plane, commonly referred to as the "spot size." These settings also determine whether an additional real crossover forms upstream of the nominal fixed crossover plane. Consequently, they strongly influence the probe current, energy width and final beam diameter at the sample. In the present experiments, we begin with a nominal spot size that corresponds to the largest spot size that does not produce an additional upstream crossover. However, because our study involves systematic variation of the extractor voltage and C1 lens settings, the manufacturer-defined spot size parameter no longer uniquely characterizes the beam conditions and should be regarded as an approximate reference only.

To create pulsed electron emission the temperature of the tip is lowered to suppress continuous thermal emission, and a pulsed laser beam is focused on the cathode to induce photoemission of electrons. In our setup we use a diode-pumped Yb-doped fiber oscillator amplifier system (Coherent Monaco 1035–40–40 LX) delivering 300 fs laser pulses at an output wavelength of 1035 nm and tunable repetition rate. We use either the 3rd or 4th harmonic of the fundamental laser beam (λ_{exc} = 345 and 258 nm, respectively), polarized along the axis of the emitter to excite the electron emitter, given that in both cases the photon energy ($E_{h\nu}$ = 3.6 eV and 4.8 eV, respectively) is larger than the work function of the tip. The laser power is altered with a variable ND filter. All experiments reported in this paper are performed using a repetition rate of 1 MHz.

While energy width measurements are routinely performed in transmission electron microscopes using commercial electron spectrometers [50], most SEMs are not equipped with energy analyzers. To enable direct measurement of the electron energy distribution, we implemented a custom retarding field analyzer (RFA) built at Delft University of Technology by Marco van der Heijden, schematically shown in Fig. 1b. The RFA is mounted on a custom translation stage inside the SEM chamber. The electron beam is directed through an entrance aperture and subsequently focused onto the retarding electrode (orange in Fig. 1b). A variable DC voltage (V_{RF}) is applied to this electrode using a high-voltage power supply (XP Power), providing retarding potentials up to 12.5 kV. By sweeping the retarding voltage and recording the transmitted electron current, the cumulative distribution function of the beam is obtained, from which the energy spectrum is extracted. Electrons transmitted through the RFA are detected using a single-electron detector (Advacam MiniPIX), enabling energy-resolved measurements of the pulsed beam.

Direct measurements of electron pulse duration are relatively common in ultrafast transmission electron microscopes (UTEMs), but are very rare in SEM-based platforms [51,52]. To characterize the temporal profile of the emitted electron pulses, we employ a dielectric laser accelerator (DLA) structure originally designed for a driving wavelength of 1.93 μm and an electron energy of 28.4 keV [33,36,41,53]. When driven at 1035 nm, phase matching is achieved via the third spatial harmonic for electrons with an energy of 10.6 keV. Under these conditions, the interaction produces an energy modulation of up to approximately 20 eV for electrons temporally overlapping with the laser pulse. (See Supplementary Information – Dielectric laser accelerators)

To measure the pulse duration, the retarding field analyzer is operated in an energy-filtering mode: the retarding voltage is set just below the nominal beam energy, such that only electrons that have gained energy within the DLA are transmitted to the detector. By varying the optical delay between the electron pulse and the driving laser, a temporal cross-correlation trace of the electron–light interaction is obtained. The intrinsic electron pulse duration is then extracted by deconvolving the measured trace with the laser pulse temporal profile.

3. Results

3.1. Charge per pulse

Fig. 2 presents measurements of the average number of electrons per pulse as a function of excitation wavelength, laser power, and electron gun settings. Fig. 2a shows the average charge per pulse obtained in USEM operation as the energy per laser pulse is varied in the pJ-nJ range, under three different gun-optics configurations and two driving wavelengths: V_{ext} = 4155 V (purple), corresponding to the default extractor setting in our instrument for thermal emission, V_{ext} = 3200 V (green) and V_{ext} = 650 V (blue), which is close to the suppressor voltage V_{supp} = 500 *V*. The intermediate extractor voltage of 3200 V is of particular practical relevance. During emitter cooldown, especially for a brand new one or one that has been running at high nominal temperature for multiple days, residual thermally driven emission can persist for extended periods. In modern systems with improved vacuum conditions, this background emission may remain measurable for hours. Reducing the extractor voltage to approximately 3000–3300 V effectively

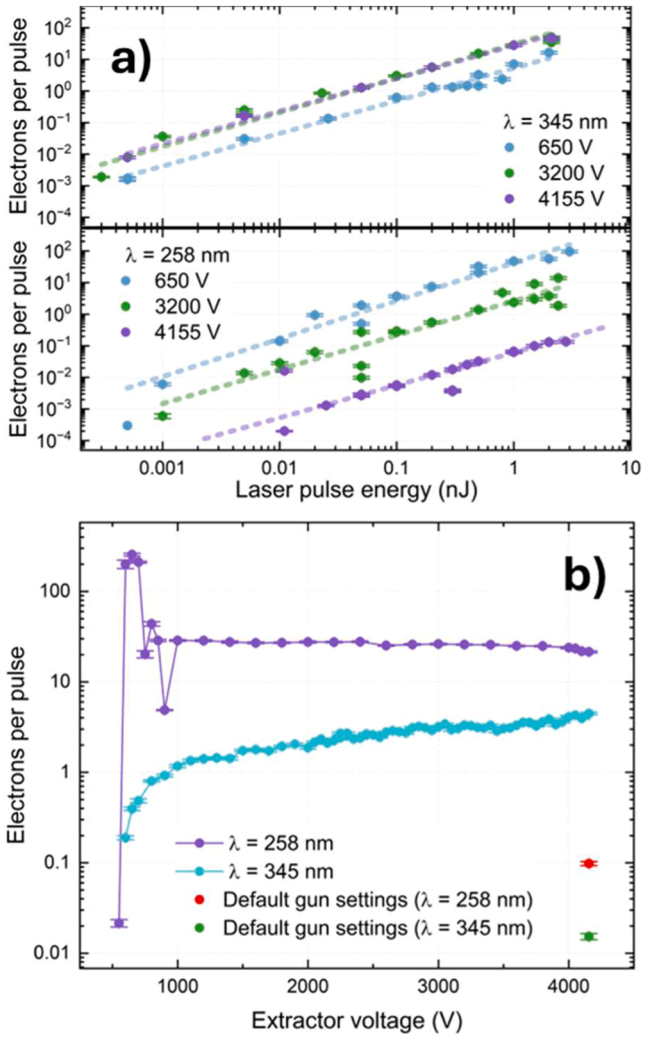

Fig. 2. Number of electrons generated per pulse at various settings. (a) Dependence on laser pulse energy while driven with 345 nm wavelength and 258 nm. Overall the current scales linearly with pulse energy at all extractor settings. (b) Dependence on extractor voltage for constant laser power. The red and green data point are for the default gun spot setting without optimization by the C1 lens voltage.

suppresses this residual thermionic contribution, enabling clean transition to purely light driven operation.

In all cases the filament current was lowered down to 1.2 A (in contrast to the nominal 2.41 A). Given that changing the extractor voltage results in a change of the effective magnification of the source, the C1 values optimized for standard (continuous) conditions are no longer valid. For this reason in order to compare properly between different extractor settings, C1, gun tilt and gun shift were tuned in each configuration to maximize the current transmitted through the aperture. In all cases, we observe that the average number of electrons per pulse increase approximately linearly when increasing the laser pulse energy.

In Fig. 2b, the laser pulse energy is held constant (2.2 nJ) while the gun settings are varied. A straightforward method to increase the transmitted current without yet changing the extractor voltage itself (default gun-specific value is 4155 V), is to adjust the C1 lens voltage. In our case, reducing C1 from 1305 V to 1100 V modifies the effective focal properties of the gun optics, thus increasing the virtual source size and moving the crossover plane closer to the aperture plane downstream. This reduces spatial filtering by the aperture and increases the transmitted beam current. Under these conditions, the average number of electrons per pulse increases by nearly two orders of magnitude. Notably, the spatial resolution changes under these settings, going from 20 nm (FWHM) to 57 nm (see Supplementary Information – Spatial resolution).

While driving the cathode with a wavelength of 345 nm (Fig. 2b - turquoise), the number of electrons per pulse decreases from 4 to 0.2 with decreasing extractor voltage from 4 to 0.6 kV. A markedly different behaviour is observed when photoemission is driven by the fourth harmonic, 258 nm (Fig. 2b - purple). While the laser-power dependence remains linear, albeit with different emission efficiency compared to 345 nm excitation, the dependence of the emitted charge on extractor voltage changes qualitatively. As the extractor voltage is reduced, the average number of electrons per pulse initially increases gradually and then rises sharply as the extractor voltage approaches the suppressor voltage (V_{supp} = 500 V). In this regime, the emitted charge reaches approximately 300 electrons per pulse. Such high-charge operation is accompanied by a significant reduction in spatial resolution and an increase in pulse duration, as discussed below. Nevertheless, this regime can be advantageous for applications where interaction areas are large, for example in electron–light interaction studies in thin SiN or Al films

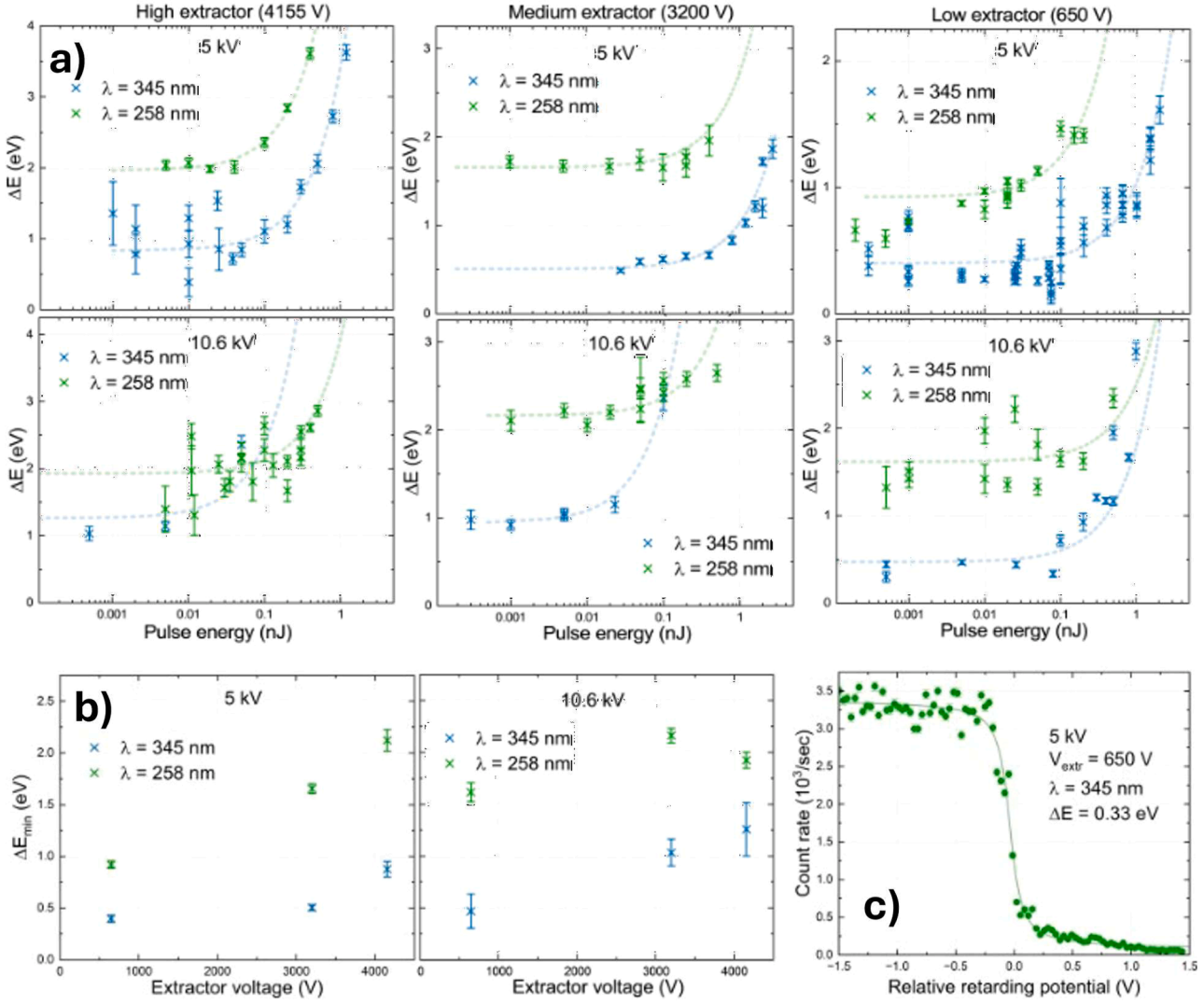

Fig. 3. Overview of the electron beam energy width (FWHM) measurements. Panel (a) shows energy width (FWHM) based on laser pulse energy, wavelength and gun voltage settings. All fits are linear functions. At low laser powers, 345 nm excitation consistently gets better energy resolution than excitation at 258 nm, while same applies for low extractor regime compared to medium and high extractor regimes across the board. The limits of energy widths from fits (i.e. intercepts of fit with pulse energy = 0 axis) are plotted in panel (b). Panel (c) shows an example of RFA type measurement fitted with cumulative distribution function of Pseudo-Voigt distribution.

[23,45], where the effective interaction area is comparable to the laser spot size, or in photonic structures operating at mid-infrared wavelengths [48], or where nonlinear material properties at high injection regimes need to be probed, for instance, performing time-resolved cathodoluminescence measurements at varying excited carrier densities to study band/trap filling, Auger recombination, and carrier screening.

The underlying mechanism arises from the interplay between collection efficiency and the effective emission barrier. Reducing the extractor voltage modifies both the field distribution near the tip and the transmission conditions through the gun optics, leading to enhanced collection efficiency despite a simultaneous increase in the emission barrier. A more detailed discussion of extractor-dependent emission efficiency is provided in the Supplementary Information – Energy barrier and Schottky effect and Supplementary Information – Electron collection efficiency.

3.2. Energy spread

Fig. 3 examines the influence of excitation wavelength and power, extractor voltage, and beam energy on the measured energy width. Fig. 3a shows a set of figures in which the measured energy width (full-width half maximum, FWHM) is plotted as a function of laser pulse energy when exciting the cathode with the third (blue) and fourth (green) harmonics. The top row shows measurements obtained with an electron acceleration voltage of 5 kV, while the bottom row corresponds to measurements at 10.6 kV. In each case, measurements were performed for three extractor settings: the default gun configuration (V_{ext} = 4155 V, left column), an intermediate extractor setting (V_{ext} = 3200 V, middle column) and a high-current low-extractor regime (V_{ext} = 650 V, right column).

In Fig. 3a, all investigated settings exhibit a qualitatively similar trend: a linear increase in energy width with increasing laser pulse energy and thus average number of electrons per pulse. The data are well fitted by linear fits (dashed curves, the apparent curvature in the plot arises from the semilogarithmic scale). This behaviour is consistent with previous works on the Boersch effect, i.e., electron–electron interactions within the bunch that broaden the longitudinal energy distribution [54–56]. These interactions are the most pronounced near the emitter, where the electrons are highly localized in both space and time and experience strong Coulomb repulsion during the early acceleration phase. As a result, both the energy spread and the transverse phase-space distribution (emittance) increase with bunch charge. For the highest pulse energies investigated here (1–2 nJ), the instantaneous current during electron emission reaches approximately 100–160 μA, comparable to the emission currents typically encountered in continuous Schottky sources. Therefore, the observed broadening can be understood within the same framework of Coulomb-driven statistical interactions, including the Boersch effect and trajectory displacement, previously studied in continuous electron beams [56].

A potential concern is the influence of the retarding field analyzer on the measured energy width. Near the cutoff voltage, electrons are significantly decelerated within the RFA, which could enhance Coulomb interactions and artificially broaden the apparent energy distribution, particularly for multi-electron pulses. We analyze this effect in detail in the Supplementary Information - Retarding field analyzer and space-charge effect) and find that it is not significant in the data range plotted in Fig. 3.

Overall, a clear trend emerges: cathode excitation at the longer wavelength

(345 nm) results in a narrower energy distribution and reducing the extractor voltage further improves the measured energy resolution. Driving the emitter with longer wavelengths leads to sub-eV energy widths (≈ 0.5–0.7 eV) at the default and intermediate extractor settings. Such narrow distributions are critical for PINEM-type experiments, where the intrinsic energy width must be significantly smaller than the photon energy to resolve discrete photon sidebands.

In our experiments (at both 5 keV and 10.6 keV acceleration energy), the smallest energy widths was achieved in the low-extractor regime, reaching values as small as 0.15 eV. This low energy width, however, comes at the expense of reduced spatial resolution due to the modified gun optics and increased beam divergence under these conditions.

From the linear fits in Fig. 3a, we can extract the energy width in the limit of zero laser pulse energy, allowing us to extract the intrinsic (charge-independent) energy width of the electron beam in the absence of space-charge broadening (ΔE_{min}). The results are shown in Fig. 3b for both electron acceleration voltages (right and left panel), extractor settings and laser wavelengths studied in Fig. 3a. The ΔE_{min} exhibits a clear decrease when decreasing the extractor voltage in nearly all cases.

Fig. 3c shows an example of a cumulative transmission curve measured with the retarding field analyzer (RFA), from which the energy distribution is obtained by differentiation.

3.3. Temporal pulse width

Another key characteristic of pulsed electron beams is the temporal pulse duration. To measure this, the electron beam was focused into the 225 nm-wide channel of the dielectric laser accelerator (DLA). An electron energy of 10.6 keV was chosen to ensure efficient phase matching with the third spatial harmonic mode at a driving wavelength of 1035 nm. In this experiment the RFA voltage is set so that barely any electrons with the primary beam energy pass through the RFA aperture. The accelerator structure accelerates the phase matched electrons, giving them a slight kick and just enough energy to overcome the potential barrier of the RFA. By varying the delay between the laser pulse and electron pulse we measure the cross-correlation signal that represents the electron beam and laser beam temporal distributions.

The measured signals are shown in Fig. 4, where both laser pulse energy driving the cathode and extractor voltage were varied. In panel (a) we show normalized cross-correlation traces for different pulse energies while driving the cathode with 258 nm light, while (b) shows the same for 345 nm excitation. Positive delays correspond to the laser arriving after the centre of the electron bunch, therefore probing the tail end of the bunch. From these traces we extract the pulse length (which we define as 2x root mean square), deconvolve the pulse length of the laser pulses and plot these in panels (c) and (d) as a function of laser pulse energy for different wavelengths and extractor voltages. Previous reports for ultrafast SEM operation at higher nominal beam energies indicate pulse durations on the order of 400 fs [57]. In our case, at lower beam energies, the pulse duration starts at approximately 500 fs at low excitation pulse energies and increases progressively with increasing laser pulse energy. Shorter pulses are generally obtained at higher extractor voltages, particularly when using third harmonic excitation. In contrast, the longest pulses, reaching up to 2 ps, are observed at high laser pulse energies under fourth harmonic excitation. In this regime, the temporal profile deviates from a Gaussian shape and exhibits a pronounced asymmetric tail. Similar asymmetric pulse shapes have been reported previously [50–52] and are attributed to collective Coulomb interactions at high charge densities close to the emitter, which distort the longitudinal phase space and preferentially decelerate electrons at the trailing edge of the bunch.

The combined dependence of charge per pulse, energy width, and pulse duration on extractor voltage and excitation wavelength reveals three distinct operating regimes for ultrafast photoemission SEM. These regimes define a practical operational space within which beam parameters can be tailored to specific experimental requirements.

(i). The first regime corresponds to high extractor voltage operation (default gun configuration). In this regime, the acceleration field at the emitter is strong, spatial resolution is optimal, and the transverse beam quality is preserved. However, the transmitted charge per pulse remains limited and residual thermionic

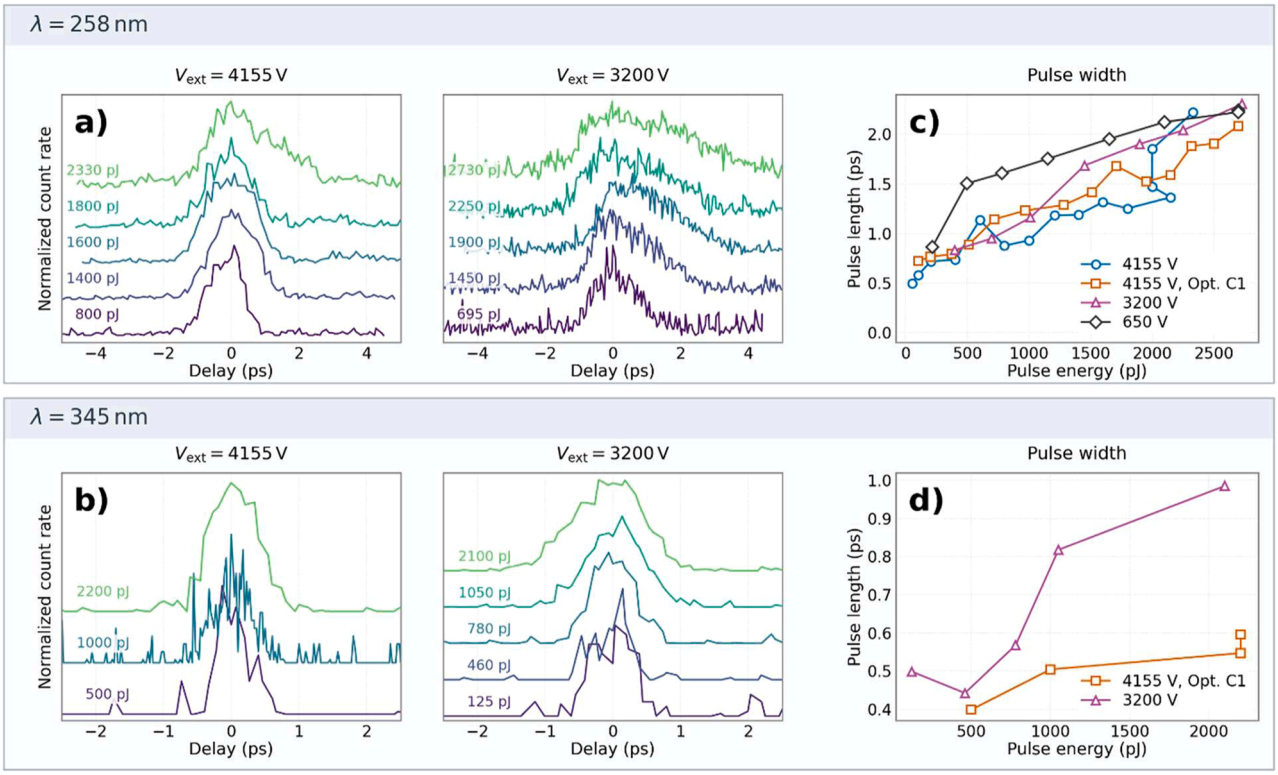

Fig. 4. Electron-light cross correlation measurements using light-electron coupling within dielectric laser accelerator structures. (a, b) Normalized count rate of electrons that gained energy as a function of relative delay between the electron and laser pulses at emitter excitation wavelengths (a) 258 nm and (b) 345 nm. (c,d) Extracted electron bunch lengths (2x RMS) after deconvolution of the 300 fs laser pulse that drives the DLA, for excitation at (c) 258 nm and (d) 345 nm.

emission can persist during emitter cooldown. This regime is therefore best suited for experiments requiring high spatial resolution and moderate beam current.

(ii). The second regime is defined by intermediate extractor voltages. Here, Schottky barrier lowering is reduced sufficiently to suppress thermionic background emission. This operating point offers a practical compromise between beam quality and narrower energy spread, in particular when driving with the third harmonic (345 nm) and is also useful when rapid transition from continuous to purely light-driven operation is required.

(iii). The third regime emerges at low extractor voltage under fourth harmonic excitation. In this configuration, the system supports significantly higher transmitted charge, reaching tens to hundreds of electrons per pulse, due to enhanced collection efficiency. At the same time, either ultralow intrinsic energy spread (<0,2 eV) or high-current operation can be achieved, depending on the excitation conditions. This regime, however, involves pronounced trade-offs, including significantly reduced spatial resolution and is achievable only with higher photon energies due to higher Schottky barrier.

Together, these regimes illustrate that ultrafast SEM operation is inherently multidimensional: optimizing charge, energy resolution, pulse duration, and spatial resolution cannot be achieved simultaneously. Instead, the appropriate operating point can be selected according to the specific demands of the experiment, whether high-resolution imaging, PINEM spectroscopy, dielectric laser acceleration, or high-charge electron–light coupling studies.

4. Conclusion

In this work, we have identified and quantitatively characterized three distinct photoemission regimes in an ultrafast SEM platform, spanning high-extractor, intermediate, and low-extractor operation at two different laser excitatiom wavelengths. These regimes define a controllable parameter space in which charge per pulse, energy spread, pulse duration, and spatial resolution can be systematically tuned, but not simultaneously optimized. High extractor operation provides optimal spatial resolution at low charge, intermediate extractor enables stable photoemission with suppressed thermionic background, and low-extractor operation under high photon energy allows access to high-charge or ultralow-energy-spread regimes at the cost of beam quality.

By systematically mapping these trade-offs, we establish practical guidelines for selecting operating conditions tailored to specific applications. This is particularly relevant for free-electron–based experiments such as PINEM spectroscopy, dielectric laser acceleration, and ultrafast electron–light interaction studies, where different regimes impose fundamentally different performance limits.

CRediT authorship contribution statement

Tomáš Chlouba: Writing – review & editing, Writing – original draft, Visualization, Validation, Supervision, Software, Resources, Methodology, Investigation, Formal analysis, Data curation, Conceptualization. **Magdalena Solà-Garcia:** Writing – review & editing, Visualization, Validation, Software, Project administration, Methodology, Investigation, Formal analysis, Data curation, Conceptualization. **Nika van Nielen:** Writing – review & editing, Visualization, Validation, Supervision, Software, Methodology, Investigation, Formal analysis, Data curation. **Matthias Wilts-Liebtrau:** Software, Methodology, Investigation, Data curation, Conceptualization. **Julian Litzel:** Resources. **Leon Brückner:** Resources. **Roy Shiloh:** Resources. **Erik Kieft:** Resources, Methodology, Investigation. **Pieter Kruit:** Supervision, Resources, Methodology, Formal analysis, Conceptualization. **Peter Hommelhoff:** Supervision, Conceptualization. **Albert Polman:** Writing – review & editing, Supervision, Project administration, Funding acquisition.

Declaration of competing interest

The authors declare that they have no known competing financial interests or personal relationships that could have appeared to influence the work reported in this paper.

Acknowledgements

This work is financed by the European Research Council (ERC) under Grant Agreement No. 101019932 (QEWS) and the European Innovation Counsel (EIC) under Grant Agreements No. 101017720 (EBEAM).

Supplementary materials

Supplementary material associated with this article can be found, in the online version, at doi:10.1016/j.ultramic.2026.114462.

Data availability

Data will be made available on request.

References

[1] R. Egerton, Physical Principles of Electron Microscopy, Springer, US, Boston, MA, 2005, https://doi.org/10.1007/b136495.
[2] C.B. Carter, D.B. Williams, Electron Microscopy, Springer International Publishing, Cham, Switzerland, 2016, https://doi.org/10.1007/978-3-319-26651-0.
[3] S. Borrelli, et al., Direct observation of sub-poissonian temporal statistics in a continuous free-electron beam with Subpicosecond resolution, Phys. Rev. Lett. 132 (2024) 115001.
[4] S. Meuret, et al., Complementary cathodoluminescence lifetime imaging configurations in a scanning electron microscope, Ultramicroscopy 197 (2019) 28–38.
[5] M. Merano, et al., Probing carrier dynamics in nanostructures by picosecond cathodoluminescence, Nature 438 (2005) 479–482.
[6] S. Sonderegger, et al., High spatial resolution picosecond cathodoluminescence of InGaN quantum wells, Appl. Phys. Lett. 89 (2006) 232109.
[7] R.J. Moerland, I.G.C. Weppelman, M.W.H. Garming, P. Kruit, J.P. Hoogenboom, Time-resolved cathodoluminescence microscopy with sub-nanosecond beam blanking for direct evaluation of the local density of states, Opt. Express. 24 (2016) 24760.
[8] M.A. Herman, D. Bimberg, J. Christen, Heterointerfaces in quantum wells and epitaxial growth processes: evaluation by luminescence techniques, J. Appl. Phys. 70 (1991) R1–R52.
[9] M. Solà-Garcia, et al., Photon statistics of incoherent cathodoluminescence with continuous and pulsed electron beams, ACS Photonics. 8 (2021) 916–925.
[10] M. Merano, et al., Probing carrier dynamics in nanostructures by picosecond cathodoluminescence, Nature 438 (2005) 479–482.
[11] M. Solà-Garcia, S. Meuret, T. Coenen, A. Polman, Electron-induced state conversion in diamond NV centers measured with pump–probe cathodoluminescence spectroscopy, ACS. Photonics. 7 (2020) 232–240.
[12] Arnaud Arbouet, Giuseppe M. Caruso, Florent Houdellier, Chapter One - Ultrafast Transmission Electron Microscopy: Historical Development, Instrumentation, and Applications, Editor(s): Peter W. Hawkes, Advances in Imaging and Electron Physics, Elsevier, Volume 207, 2018, Pages 1-72, ISSN 1076-5670, ISBN 9780128152157, https://doi.org/10.1016/bs.aiep.2018.06.001.
[13] L. Zhang, J.P. Hoogenboom, B. Cook, P. Kruit, Photoemission sources and beam blankers for ultrafast electron microscopy, Struct. Dyn. 6 (2019) 051501.
[14] A. Gahlmann, S. Tae Park, A.H. Zewail, Ultrashort electron pulses for diffraction, crystallography and microscopy: theoretical and experimental resolutions, Phys. Chem. Chem. Phys. 10 (2008) 2894.
[15] F. Houdellier, et al., Optimization of off-axis electron holography performed with femtosecond electron pulses, Ultramicroscopy 202 (2019) 26–32.
[16] A.H. Zewail, Four-Dimensional electron microscopy, Science (1979) 328 (2010) 187–193.
[17] H.S. Park, J.S. Baskin, O.-H. Kwon, A.H. Zewail, Atomic-Scale imaging in real and energy space developed in ultrafast electron microscopy, Nano Lett. 7 (2007) 2545–2551.
[18] B. Barwick, D.J. Flannigan, A.H. Zewail, Photon-induced near-field electron microscopy, Nature 462 (2009) 902–906.
[19] S.T. Park, M. Lin, A.H. Zewail, Photon-induced near-field electron microscopy (PINEM): theoretical and experimental, New. J. Phys. 12 (2010) 123028.
[20] R. Shiloh, T. Chlouba, P. Hommelhoff, Quantum-Coherent light-electron interaction in a scanning electron microscope, Phys. Rev. Lett. 128 (2022) 235301.
[21] A. Feist, et al., Quantum coherent optical phase modulation in an ultrafast transmission electron microscope, Nature 521 (2015) 200–203.
[22] F.J. Garcia De Abajo, A. Asenjo-Garcia, M. Kociak, Multiphoton absorption and emission by interaction of swift electrons with evanescent light fields, Nano Lett. 10 (2010) 1859–1863.
[23] G.M. Vanacore, et al., Attosecond coherent control of free-electron wave functions using semi-infinite light fields, Nat. Commun. 9 (2018) 2694.
[24] T. Bucher, et al., Coherently amplified ultrafast imaging using a free-electron interferometer, Nat. Photonics. 18 (2024) 809–815.
[25] A. Feist, et al., Cavity-mediated electron-photon pairs, Science (1979) 377 (2022) 777–780.
[26] O. Reinhardt, C. Mechel, M. Lynch, I. Kaminer, Free-Electron Qubits, Ann. Phys. 533 (2021) 2000254, https://doi.org/10.1002/andp.202000254.
[27] M. Sirotin, A. Rasputnyi, T. Chlouba, R. Shiloh, P. Hommelhoff, Quantum Opt. Recoiled Free Electrons (2024). http://arxiv.org/abs/2405.06560.
[28] R. Ruimy, A. Karnieli, I. Kaminer, Free-electron quantum optics, Nat. Phys. 21 (2025) 193–200.
[29] N. Schönenberger, et al., Generation and characterization of attosecond Microbunched electron pulse trains via dielectric laser acceleration, Phys. Rev. Lett. 123 (2019) 264803.
[30] K.E. Priebe, et al., Attosecond electron pulse trains and quantum state reconstruction in ultrafast transmission electron microscopy, Nat. Photonics. 11 (2017) 793–797.
[31] D.S. Black, et al., Net acceleration and direct measurement of attosecond electron pulses in a silicon dielectric laser accelerator, Phys. Rev. Lett. 123 (2019) 264802.
[32] J. Breuer, P. Hommelhoff, Laser-Based acceleration of nonrelativistic electrons at a dielectric structure, Phys. Rev. Lett. 111 (2013) 134803.
[33] R. Shiloh, T. Chlouba, P. Yousefi, P. Hommelhoff, Particle acceleration using top-illuminated nanophotonic dielectric structures, Opt. Express. 29 (2021) 14403.
[34] U. Niedermayer, T. Egenolf, O. Boine-Frankenheim, P. Hommelhoff, Alternating-Phase focusing for dielectric-laser acceleration, Phys. Rev. Lett. 121 (2018) 214801.
[35] T. Chlouba, et al., Coherent nanophotonic electron accelerator, Nature 622 (2023) 476–480. *622:7983*.
[36] P. Yousefi, et al., Dielectric laser electron acceleration in a dual pillar grating with a distributed Bragg reflector, Opt. Lett. 44 (2019) 1520.
[37] M. Kozák, et al., Dielectric laser acceleration of sub-relativistic electrons by few-cycle laser pulses, Nucl. Instrum. Methods Phys. Res. A 865 (2017) 84–86.
[38] J. McNeur, et al., Elements of a dielectric laser accelerator, Optica 5 (2018) 687.
[39] R. Shiloh, et al., Miniature light-driven nanophotonic electron acceleration and control, Adv. Opt. Photonics. 14 (2022) 862.
[40] R.J. England, et al., Dielectric laser accelerators, Rev. Mod. Phys. 86 (2014) 1337–1389.
[41] K.J. Leedle, et al., Dielectric laser acceleration of sub-100 keV electrons with silicon dual-pillar grating structures, Opt. Lett. 40 (2015) 4344.
[42] N.V. Sapra, et al., On-chip integrated laser-driven particle accelerator, Science (1979) 367 (2020) 79–83.
[43] E.A. Peralta, et al., Demonstration of electron acceleration in a laser-driven dielectric microstructure, Nature 503 (2013) 91–94.
[44] P. Broaddus, et al., Subrelativistic alternating phase focusing dielectric laser accelerators, Phys. Rev. Lett. 132 (2024) 085001.
[45] Y. Morimoto, P. Baum, Diffraction and microscopy with attosecond electron pulse trains, Nat. Phys. 14 (2018) 252–256.
[46] A. Ryabov, J.W. Thurner, D. Nabben, M.V. Tsarev, P. Baum, Attosecond metrology in a continuous-beam transmission electron microscope, Sci. Adv. 6 (2020) eabb1393.
[47] M. Tsarev, J.W. Thurner, P. Baum, Nonlinear-optical quantum control of free-electron matter waves, Nat. Phys. 19 (2023) 1350–1354.
[48] L. Brückner, et al., Mid-infrared dielectric laser acceleration in a silicon dual pillar structure, Opt. Express. 32 (2024) 28348.
[49] M. Kozák, T. Eckstein, N. Schönenberger, P. Hommelhoff, Inelastic ponderomotive scattering of electrons at a high-intensity optical travelling wave in vacuum, Nat. Phys. 14 (2018) 121–125.
[50] N. Bach, et al., Coulomb interactions in high-coherence femtosecond electron pulses from tip emitters, Struct. Dyn. 6 (2019) 1014301.
[51] M. Kozák, et al., Ultrafast scanning electron microscope applied for studying the interaction between free electrons and optical near-fields of periodic nanostructures, J. Appl. Phys. 124 (2018) 023104.
[52] K. Moriová, P. Koutenský, M.-C. Chirita-Mihaila, M. Kozák, Temporal characterization of femtosecond electron pulses inside ultrafast scanning electron microscope, Rev. Sci. Instrum. 96 (2025).
[53] P. Koutenský, et al., Ultrafast 4D scanning transmission electron microscopy for imaging of localized optical fields, ACS. Photonics. 12 (2025) 4452–4459.
[54] D.A. Plemmons, D.J. Flannigan, Ultrafast electron microscopy: instrument response from the single-electron to high bunch-charge regimes, Chem. Phys. Lett. 683 (2017) 186–192.
[55] K. Bücker, et al., Electron beam dynamics in an ultrafast transmission electron microscope with Wehnelt electrode, Ultramicroscopy 171 (2016) 8–18.
[56] M. Bronsgeest, Physics of Schottky electron Sources, Delft University of Technology, 2009, ISBN 978-90-8570-434-8.
[57] M. Kozák, et al., Ultrafast scanning electron microscope applied for studying the interaction between free electrons and optical near-fields of periodic nanostructures, J. Appl. Phys. 124 (2018) 1–10.